Title
Modeling of emittance growth due to Coulomb collisions in plasma-based accelerators

Journal
Physics of Plasmas, 27(11)

ISSN
1070-664X

Authors
Zhao, Y
Lehe, R
Myers, A
et al.

Publication Date
2020-11-01

DOI
10.1063/5.0023776

Peer reviewed

Modeling of Emittance Growth Due to Coulomb Collisions in Plasma-based Accelerators

Y. Zhao,[1, a)] R. Lehe,[1] A. Myers,[1] M. Thévenet,[1] A. Huebl,[1] C. B. Schroeder,[1, 2] and J.-L. Vay[1]
[1)]*Lawrence Berkeley National Laboratory, Berkeley, California 94720, USA*
[2)]*Department of Nuclear Engineering, University of California, Berkeley, California 94720, USA*

(Dated: 21 October 2020)

Coulomb collisions with background plasma are one source of emittance degradation in plasma accelerators. This paper shows that the emittance growth due to Coulomb collisions can be correctly captured in particle-in-cell simulations, with a proper Monte Carlo binary collision module. The theory of the emittance growth due to Coulomb collisions is extended from a monoenergetic matched beam to a mismatched beam with energy spread, and is compared with simulation results.

I. INTRODUCTION

In many applications of plasma-based accelerators, the beam quality is crucial. For example, future high-energy colliders based on laser-wakefield acceleration (LWFA)[1] will require a small beam transverse size to obtain a high luminosity. Similarly, prospective LWFA-based free-electron lasers (FEL)[2–4] require both a small beam transverse size to preserve high current density and a low beam divergence to maintain coherence. These constraints could generally be obtained by preserving the emittance of an initial high-quality beam, throughout its acceleration.

However, the emittance is not guaranteed to be preserved in a plasma-based accelerator. Potential sources of emittance degradation include decoherence of a mismatched beam[5,6] or misaligned beam[5,7], non-linear focusing fields (e.g. resulting from ion motion in the plasma wakefield)[8–10], and beam-hosing instability[11–16]. Another source of emittance degradation, which is perhaps less commonly considered, is the Coulomb collisions with the background plasma. Analytical calculations of emittance growth due to Coulomb collisions in plasma-based accelerators were first introduced by Montague and Schnell in 1985[17], in which the calculation is based on, and extended from, the well established formulas for angular scatter in a neutral vapor. Later, the formalism was also applied to calculate quantitatively the emittance growth due to Coulomb collisions in the blowout beam-driven regime[18] and the quasi-linear laser-driven regime[1], including in near-hollow plasma channels[19].

These previous analytical derivations of emittance growth due to Coulomb collisions[1,18,19], are based on simplifying assumptions, including matched and monoenergetic beam. In order to study more complicated situations, appropriate numerical tools are needed to carry out corresponding simulations. In this paper, it is shown that emittance growth due to Coulomb collisions can be correctly captured in particle-in-cell (PIC) simulations, with a proper Monte Carlo binary collision module. In addition, the module can help to extend the theory to more complicated situations, such as mismatched beams.

[a)]Electronic mail: yinjianzhao@lbl.gov

The paper is organized as follows. In Sec. II, we summarize how Coulomb collisions are modeled theoretically and in PIC simulations. In particular, we emphasize the similarities and differences in the assumptions that underpin these two descriptions. In Sec. III, we compare the analytical predictions and the numerical simulations in several situations, including a plasma-accelerator configuration. At last, conclusions are drawn and possible future works are discussed in Sec. IV.

II. ANALYTICAL AND NUMERICAL DESCRIPTION OF THE GROWTH OF EMITTANCE FROM COULOMB COLLISIONS.

In this section, we summarize how Coulomb collisions are modeled in the standard analytical theory[1,18] and in PIC simulations[20], and how the corresponding growth of emittance is computed.

A. Analytical description

Let us consider a relativistic beam of electrons, propagating along the z axis, through a background of ion particles at rest (having charge $q = Ze$ and uniform density n). Each electron of the beam undergoes multiple Coulomb collisions during the propagation, which result in small, random deviations in the angles θ_x and θ_y. As a result, a given electron will have a probability distribution in θ_x, θ_y, which will widen with time (i.e. $\langle\theta_x^2\rangle$ and $\langle\theta_y^2\rangle$ increase with time).

The growth rate of the width of this probability distribution can be computed analytically[21]. (For the convenience of the reader, we include a detailed derivation in Appendix A.) The calculation results in $d\langle\theta_x^2\rangle/dt = d\langle\theta_y^2\rangle/dt = (1/2)d\langle\theta^2\rangle/dt$, with:

$$\frac{d\langle\theta^2\rangle}{dt} = \frac{8\pi n r_e^2 c}{\gamma^2} Z^2 \ln\Lambda, \tag{1}$$

where γ is the Lorentz factor of the electron, Ze and n are the charge and density of the background ion particles, c is the vacuum speed of light, t is the time, $r_e \approx 2.82 \times 10^{-15}$ m is the classical electron radius, and $\ln\Lambda$ is the Coulomb logarithm[21], which takes into account the typical distance over which

Coulomb interactions are screened. The Coulomb logarithm will be discussed in more detail in section II C.

These collisions introduce disorder in the beam: instead of forming a well-collimated beam, individual electrons scatter in different directions, and, as a result, the emittance increases. The growth of emittance can be calculated by considering the equations of motion of individual electrons (e.g., in a focusing plasma bubble), and averaging them over the whole beam to obtain a set of envelope equations. In this case, the random change in angle due to Coulomb collisions [expressed by Eq. (1)] is taken into account by adding a stochastic noise term in the individual equations of motion. (In other words, the equations of motion become Langevin equations.) This procedure is detailed in Appendix B. The resulting expression for the growth of emittance (e.g. in the x direction) is:

$$\frac{d\varepsilon_x^2}{dz} = k_p^2 r_e Z \ln\Lambda \langle x^2\rangle + 2\left(\langle u_x^2\rangle \left\langle \frac{x u_x}{\gamma}\right\rangle - \langle x u_x\rangle \left\langle \frac{u_x^2}{\gamma}\right\rangle\right), \tag{2}$$

where $k_p^2 = 4\pi Z n r_e$ corresponds to the plasma wavenumber, and the brackets $\langle ...\rangle$ indicate an average over the whole beam, with x the transverse position of an individual electron $u_x = p_x/(m_e c)$ its dimensionless momentum, and the emittance is defined as $\varepsilon_x^2 \equiv \langle x^2\rangle\langle u_x^2\rangle - \langle x u_x\rangle^2$. Note that the right-hand side of Eq. (2) contains two contributions to emittance growth: a first term from the Coulomb collisions, and the second term from the decoherence associated with energy spread[5].

As expected, in the particular case of a matched, monoenergetic beam, Eq. (2) reduces to previous results from the literature[1,18]. More specifically, in the case of a monoenergetic beam, the second term in the right-hand side of Eq. (2) cancels. Moreover, for a matched beam in the bubble regime, we have $\varepsilon_x = \sqrt{\gamma/2}k_p\langle x^2\rangle$, and thus Eq. (2) can be written as:

$$\frac{d\varepsilon_x}{dz} = \frac{k_p^2 r_e Z \ln\Lambda \langle x^2\rangle}{2\varepsilon_x} = \frac{k_p r_e Z \ln\Lambda}{\sqrt{2\gamma}}. \tag{3}$$

For a mismatched beam, we can obtain $\langle x^2\rangle$ from the envelope equation under a linear focusing force,

$$\langle x^2\rangle = \frac{1}{2}\left(x_m^2 + \frac{\varepsilon_x^2}{\gamma^2 k_\beta^2 x_m^2}\right), \tag{4}$$

where x_m^2 is the peak value of $\langle x^2\rangle$, $k_\beta = k_p(2\gamma)^{-1/2}$ is the betatron oscillation wave number. Detailed derivation is given in Appendix B.

While the first term of Eq. (2) can be readily evaluated through Eq. (4), the second term of Eq. (2) on the other hand depends on $\langle x u_x\rangle$, $\langle x u_x/\gamma\rangle$, $\langle u_x^2\rangle$, and $\langle u_x^2/\gamma\rangle$ which require additional information (e.g., an additional model) to be evaluated. In this paper, for simplicity, we obtain these values numerically from simulations.

B. Numerical description in a PIC code

In this section, we summarize the PIC implementation of Coulomb collisions described in Perez et al.[20], and highlight the similarities and differences in section II A. This implementation extends earlier work by Nanbu[22,23], and is the one used in the rest of this paper.

In this implementation, Coulomb collisions are considered whenever two macroparticles are in the same cell. Conceptually, these macroparticles represent two fluxes of physical particles that collide with each other, whereby each individual physical particle from one macroparticle undergoes multiple scatterings with the physical particles from the other macroparticle. As a result of these collisions, the RMS divergence associated with these groups of physical particles should (conceptually) increase. If we label the two macroparticles with the index 1 and 2 respectively, the increase in RMS divergence associated with macroparticle 1 is:

$$\frac{d\langle\theta_1^{*2}\rangle}{dt} = \frac{\gamma_c p_1^*}{\gamma_1\gamma_2(\gamma_1 m_1 + \gamma_2 m_2)} 8\pi n_2 r_e^2 \left(\frac{q_1 q_2}{e^2}\right)^2 \left(\frac{m_e^2}{m_1 m_2}\right)\left(\frac{\gamma_1^* m_1 \gamma_2^* m_2}{p_1^{*2}} c^2 + 1\right)^2 \ln\Lambda. \tag{5}$$

(See Perez et al.[20] for a derivation, which is based on the relativistic Frankel cross-section[24] ; note that, in the derivation from Perez et al., the quantity s_{12} corresponds to $\Delta t/2 \times d\langle\theta_1^{*2}\rangle/dt$ here.) In the above expression, q_1, m_1, γ_1 and q_2, m_2, γ_2 are the charge, mass and Lorentz factor of the individual physical particles represented by the macroparticles 1 and 2 respectively, and n_2 is the density associated with the macroparticle 2 in the current cell (i.e., weight divided by cell volume). Quantities denoted with a star are taken in the *center-of-mass frame of the collision*, and γ_c is the Lorentz factor associated with this frame. In particular, θ_1^* is the scattering angle with respect to the initial propagation direction of macroparticle 1, *in the center-of-mass frame*.

It is important to note, however, that in the standard PIC scheme, macroparticles cannot carry an intrinsic RMS divergence, since they have a unique, well-defined velocity vector. Therefore, in the implementation by Perez et al. (as well as in the earlier implementation by Nanbu), the scattering angle for the whole macroparticle is sampled in a Monte Carlo fashion, so as to reproduce Eq. 5 on average.

More specifically, for a collision between two macroparticles occurring over one timestep Δt, the RMS divergence $\Delta t \times d\langle\theta_1^{*2}\rangle/dt$ is calculated from Eq. (5), and a specific value θ_1^* is sampled from a probability distribution that reproduces this RMS divergence. The momentum of the incident macroparticle 1 is then transformed to the center-of-mass frame, rotated by the angle θ_1^*, and transformed back to the frame of the simulation.

There are important similarities between the collision model used in the simulation [i.e., Eq. (5)] and in the analytical theory [i.e., Eq. (1)], and these will be discussed further in section II C. However, one significant difference is that the model used in the analytical theory [Eq. (1)] assumes the background particles to be at rest, i.e, immobile ions, while the model used in the simulation [Eq. (5)] is fully generic with respect to the velocity of macroparticle 2. (Incidentally, it can easily be verified that Eq. (5) reduces to Eq. (1), in the particular case where the macroparticle 2 is at rest and has large mass $m_2 \gg \gamma_1 m_1$, such that the center-of-frame mass is identical to the frame of the simulation.) Since Eq. (5) is fully relativistic and fully generic with respect to velocities, we can directly use the corresponding collision module in boosted-frame simulations[25] of plasma acceleration, where e.g. the background ions are indeed *not* at rest in the frame of the simulation. This is important, because growth of emittance typically needs to be evaluated over long acceleration distances, and the boosted-frame technique can then drastically reduce the cost of these simulations.

C. Approximations and limitations

The collision models used in the analytical theory (section II A) and the numerical simulation (section II B) both rely on significant assumptions. It is important to be aware of these assumptions when applying these models.

One of these assumptions is that there is an effective screening distance b_{max} beyond which Coulomb interactions between two particles are suppressed (as well as an effective minimal impact parameter b_{min}).[24] This effectively translates into the presence of the Coulomb logarithm in Eq. (1) and Eq. (5), with $\ln\Lambda = \ln(b_{max}/b_{min})$. In the context of general plasma physics, b_{max} is usually taken to be the Debye length λ_D (and b_{min} is given, e.g., in Perez et al.[20]). However, in the context of plasma acceleration in the bubble regime, Kirby et al.[18] propose to use the bubble radius as b_{max}, and the effective Coulombic radius of the nucleus $R \approx 1.4A^{1/3}$ fm as b_{min}. While more work is certainly needed in order to obtain a rigorous estimation of the Coulomb logarithm, in this paper, for the purpose of comparing theory and simulation, we choose $\ln\Lambda = \ln(\lambda_D/R)$. Importantly, we use the same value both in the theory and simulation.

Another important assumption of the collision models is that the background plasma is uniform over the characteristic screening distance b_{max}. For instance, in the model used for the analytical theory Eq. (1), it is assumed that the plasma density n is uniform over the screening distance b_{max}. Similarly, when applying the collision module from section II B in PIC simulations, it is assumed that the density and velocity distribution of the macroparticles of the *current cell* are representative of the density and velocity distribution over the screening distance b_{max}. Importantly, this assumption is violated for instance in the case of hollow-channel plasma acceleration[19], where Coulomb collisions occur with the non-uniform plasma in the walls of the channel. (It is worthwhile to note that Eq. (1) can nonetheless be generalized[19] to the case of a transversely-varying plasma.) Finally, in the case of the bubble regime, the assumption of uniformity is valid for the background plasma ions, but not for the plasma electrons. However, it is generally considered that Coulomb collisions with the plasma electrons (e.g., in the bubble sheath) is negligible compared to Coulomb collisions with the plasma ions (which fill the bubble), and in the rest of this paper, we only consider collisions with the ions.

In the case of the numerical simulation, it is important to note that the PIC algorithm itself also captures the Coulomb interaction between macroparticles, as long as they are separated by more than a few cells. Therefore, for particles that are separated by more than the cell size (but less than b_{max}), Coulomb collisions are in principle doubled-counted, since they are taken into account both by the PIC algorithm itself, and by the collision module. A detailed study of this double-counting effect would certainly be of utmost interest. However, in this paper, we found no evidence that double-counting had a significant effect, when comparing the analytical theory (which does not feature double-counting) and the numerical simulations. This is because, for the parameters used in this paper, $\lambda_D < \Delta x$ (cell size), and the impact of collisions between particles separated by more than a cell size is in fact negligible compared to the impact of collisions occurring within a cell.

III. SIMULATION BENCHMARKS

In this section, PIC simulations of two setups are carried out, and simulation results are compared with the analytical solutions. All simulations in this work are done using the open-source particle-in-cell code WarpX[26]. The major modules of WarpX that are used in the simulations of this work are Pérez's Monte Carlo binary collision model[20], Cole-Karkkainen Maxwell solver with Cowan coefficients[27], Boris's particle pusher[28], Berenger's perfectly matched layers[29], and the Lorentz boosted frame technique[30].

A. Simplified configuration: Beam propagating in a uniform ion background

In order to perform a direct comparison between the theory and simulations, a simple pure collision setup is first considered. No field solver is used in this setup (i.e., the fields on the grids are zero), and only Coulomb collisions (using the above-mentioned module) are considered. A 3D cubic simulation domain is used with size $300 \times 300 \times 300$ μm, and number of cells $8 \times 8 \times 8$, in x, y, and z direction, respectively. A beam of electrons with total charge -5 pC, represented by 10^5 macro-particles, is initially placed at the center of the domain. The beam has a relativistic velocity in z, with a Lorentz factor $\langle\gamma\rangle = 200$. Plasma ions are uniformly distributed in the domain, with a number density $n_i = 10^{18}$ cm^{-3}, charge number $Z = 1$, and mass number $A = 1$. One macro-particle per cell is used for ions. Assuming a constant plasma temperature $T_i = T_e = 10$ eV, we can obtain $k_p \approx 1.88 \times 10^5$ rad/m,

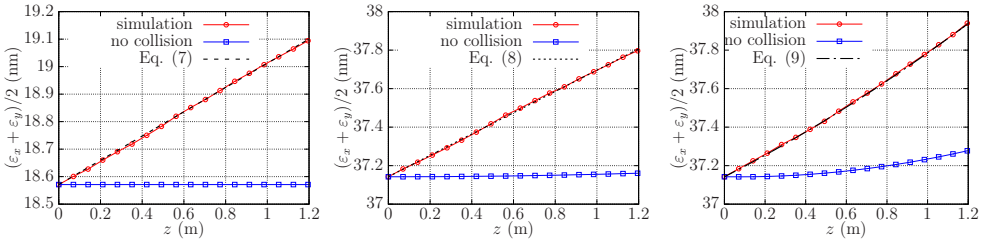

FIG. 1. Emittance ε as a function of z, for a monoenergetic matched beam with $\sigma_{x,y} = 0.1\ \mu m$ (left), a monoenergetic mismatched beam with $\sigma_{x,y} = 0.2\ \mu m$ (middle), a mismatched beam with $\sigma_{x,y} = 0.2\ \mu m$ and energy spread $\sigma_{uz} = 0.002$ (right). Dashed curves are analytical predictions.

$k_\beta \approx 9410$ rad/m, $\lambda_D \approx 23.5$ nm, thus the Coulomb logarithm $\ln\Lambda \approx 16.6$. Ions are set to be fixed during the whole simulation. Plasma electrons are not simulated. To focus the beam, an external focusing electric field that emulates the fields of a plasma bubble is added,

$$E_x = E_0 x, \qquad E_y = E_0 y, \tag{6}$$

where $E_0 = m_e c^2 k_p^2/(2e) \approx 9.05\times10^{15}$ V/m^2. A moving window is applied along z with the speed of light. Only the collisions between beam electrons and plasma ions are considered, with the above-mentioned fixed Coulomb logarithm. The Boris algorithm[31], a second-order leapfrog integrator of the equations of motion, is used to push particles. The simulation time step is set to $\Delta t \approx 1.56\times10^{-14}$ s.

In the simulations, the electron beam has a Gaussian distribution in phase space. In order to test the code and theory in different regimes, we varied the RMS sizes of this distribution, so as to consider three different cases:

- a monoenergetic matched beam, with $\sigma_x = \sigma_y = \sigma_z = 0.1\ \mu$m, $\sigma_{ux} = \sigma_{uy} = \gamma k_\beta \sigma_x$, and $\sigma_{uz} = 0$.
- a monoenergetic mismatched beam, with the same momentum distribution as the matched beam, but a larger transverse size: $\sigma_x = \sigma_y = 0.2\ \mu$m,
- a mismatched beam with $\sigma_x = \sigma_y = 0.2\ \mu$m as in the previous case and an energy spread: $\sigma_{uz} = 0.002$.

The three different cases are represented by the three panels in Fig. 1.

For each of these three different cases, the simulated growth of the mean emittance $(\varepsilon_x+\varepsilon_y)/2$ is shown in Fig. 1 (red line). Since the beam is axisymmetric about z, we plot $(\varepsilon_x+\varepsilon_y)/2$, for the purpose of reducing the statistical particle noise. For comparison, we also ran the same simulations with the collision module turned off (blue lines). As expected, these curve show no growth of emittance in the cases with monoenergetic beams.

The simulated growth of emittance with collisions (red lines) is also compared with the analytical predictions Eq. (2) and Eq. (3). More specifically, in order to plot the black lines in Fig. 1, we use the following discretization

$$\varepsilon_x(z+\Delta z) = \varepsilon_x(z) + \frac{k_p r_e Z \ln\Lambda}{\sqrt{2\tilde{\gamma}}}\Delta z \tag{7}$$

for the monoenergetic matched beam,

$$\varepsilon_x(z+\Delta z) = \varepsilon_x(z) + \frac{k_p^2 r_e Z \ln\Lambda}{4\varepsilon_x(z)}\left(x_m^2 + \frac{\varepsilon_x^2(z)}{\gamma^2 k_\beta^2 x_m^2}\right)\Delta z \tag{8}$$

for monoenergetic mismatched beam [from Eq. (2) without energy spread], and

$$\varepsilon_x(z+\Delta z) = \varepsilon_x(z) + \frac{k_p^2 r_e Z \ln\Lambda \langle x^2\rangle}{4\varepsilon_x(z)}\left(x_m^2 + \frac{\varepsilon_x^2(z)}{\gamma^2 k_\beta^2 x_m^2}\right)\Delta z + \frac{\langle u_x^2\rangle\langle x u_x/\gamma\rangle - \langle x u_x\rangle\langle u_x^2/\gamma\rangle}{\varepsilon_x(z)}\Delta z \tag{9}$$

for the mismatched beam with energy spread [from Eq. (2)], where γ, $\langle u_x^2\rangle$, $\langle x u_x\rangle$, $\langle x u_x/\gamma\rangle$, and $\langle u_x^2/\gamma\rangle$ are all functions of z, obtained from the simulation, and $x_m = \sigma_x = 0.2\ \mu$m.

Each of the three cases display excellent agreement with the corresponding theoretical curve in Fig. 1, thereby validating the implementation of the collision module.

B. Plasma accelerator

We now consider a simulation of beam-driven plasma accelerator. The simulation is run in a boosted frame[25] with Lorentz factor $\gamma_b = 10$. A 3D cubic simulation domain is used, with $64\times64\times256$ cells in x, y, and z, respectively, and the physical domain size corresponds to a 200 $\mu m \times 200\ \mu m \times 256\ \mu m$ box in the lab-frame.

The boundary condition is periodic in x and y, and open in z. A driver electron beam is initialized with a charge of -1 nC, represented by 1000 macro-particles, and a Gaussian distribution with $\sigma_x = \sigma_y \approx 6.32\ \mu$m, $\sigma_z \approx 12.65\ \mu$m, $\sigma_{ux} = \sigma_{uy} = 2$, $\sigma_{uz} = 2\times10^4$, $\langle u_x\rangle = \langle u_y\rangle = 0$, $\langle u_z\rangle = 2\times10^7$. We set an artificially high mass of 10^{10} kg and high $\langle u_z\rangle$ for the particles of the driver beam, to impose rigidity.

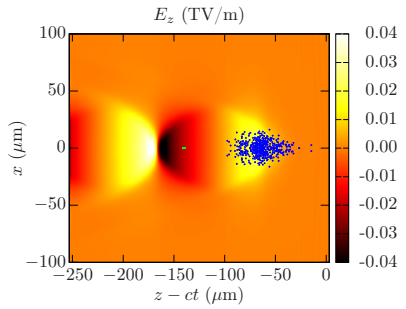

FIG. 2. Plots of E_z with beam (green dots) and driver (blue dots) at $t \approx 33$ fs.

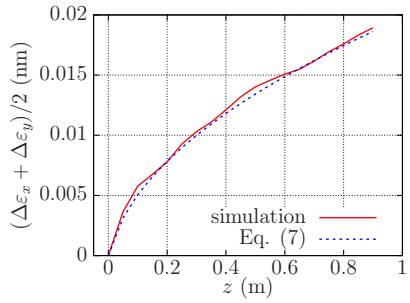

FIG. 3. Emittance growth $\Delta\varepsilon$ versus propagation distance z.

A witness beam of electrons with total charge -5 pC, represented by 10^6 macro-particles, is placed 77 μm behind the driver. The witness beam has a Gaussian distribution in phase-space, with $\sigma_x = \sigma_y = \sigma_z \approx 0.316$ μm, $\sigma_{ux} = \sigma_{uy} \approx 0.188$, $\sigma_{uz} = 0$, $\langle u_x \rangle = \langle u_y \rangle = 0$, and $\langle u_z \rangle = 200$.

Plasma ions and electrons have a density profile

$$n_{e,i} = \begin{cases} (1 - \cos\dfrac{\pi z}{L})\dfrac{n_0}{2}, & \text{if } z < L \\ n_0, & \text{if } z \geq L \end{cases}$$

where $n_0 = 10^{17}$ cm^{-3}, $L = 1$ mm. Ion charge number is $Z = 1$ and mass number is $A = 1$. Both electrons and ions have a Gaussian velocity distribution with temperature $T_e = T_i = 10$ eV. One macro-particle per cell is used for electrons and ions. Under these parameters, the Coulomb logarithm is $\ln\Lambda \approx 17.8$. The electromagnetic fields are solved by the Cole-Karkkainen solver with Cowan coefficients[32]. A moving window is applied along z with the speed of light. Again, only the collisions between beam electrons and plasma ions are considered, with the above-mentioned fixed Coulomb logarithm. The simulation time step is set to $\Delta t \approx 0.165$ fs (3.3 fs in the boosted frame). Collisions are computed at every time step.

The simulation setup is illustrated in Fig. 2, which displays a snapshot of the electric field at $t \approx 33$ fs (in the lab frame). For this setup, γ of the beam increases linearly during the simulation and reaches about 33×10^3 at the end when the beam reaches $z \approx 0.96$ m. The emittance growth due to collisions $\Delta\varepsilon$ is shown in Fig. 3. We can see that, again the simulation result matches with the theory for a matched beam.

IV. CONCLUSIONS AND FUTURE WORK

This paper shows that the emittance growth due to Coulomb collisions in plasma-based accelerators can be correctly captured in particle-in-cell (PIC) simulations, with a proper Monte Carlo binary collision module implemented. In addition, the theory of the emittance growth due to Coulomb collisions is generalized to describe a mismatched beam with energy spread, and simulation results match the corresponding theory. In the future, the emittance growth due to Coulomb collisions in the linear regime of plasma-based accelerators will be explored theoretically and numerically.

ACKNOWLEDGMENTS

The authors would like to thank D. Amorim, C. Benedetti, S. Bulanov, E. Esarey, C. Geddes, M. Rowan S. Steinke, and E. Zoni for useful discussions and comments, and all WarpX contributors. The authors would also like to acknowledge discussions with F. Pérez on the implementation of the collision module. This research was supported by the Exascale Computing Project (17-SC-20-SC), a collaborative effort of the U.S. Department of Energy Office of Science and the National Nuclear Security Administration. This work was supported by the Director, Office of Science, Office of High Energy Physics, U.S. Dept. of Energy under Contract No. DEAC02-05CH11231.

DATA AVAILABILITY

The data that support the findings of this study are available at Zenodo[33].

Appendix A: Derivation of Coulomb scattering for a monoenergetic matched beam in the blown-out regime

Consider a binary collision between an electron and a fixed ion in the x-z plane, as shown in Fig. 4. The impact parameter is b, the scattering angle is θ, electron's initial momentum is $\boldsymbol{p}_1 = (0, p) = \gamma m_e \boldsymbol{v}$. And the electron's final momentum after the collision is $\boldsymbol{p}_2 = (p\sin\theta, p\cos\theta)$.

Thus, we can find the momentum change

$$|\Delta p|^2 = |\boldsymbol{p}_2 - \boldsymbol{p}_1|^2 = 4p^2 \sin^2\frac{\theta}{2}, \tag{A1}$$

where $1 - \cos\theta = 2\sin^2(\theta/2)$ is used.

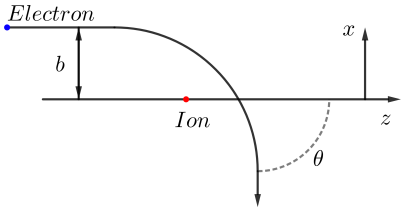

FIG. 4. Binary collision plane.

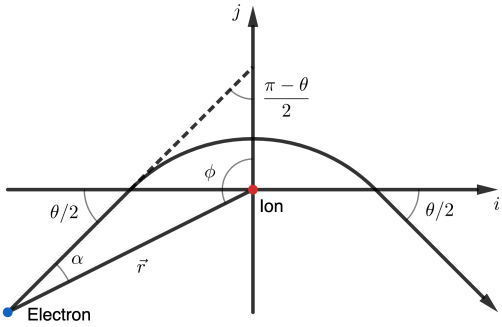

FIG. 5. Symmetric binary collision plane.

If we change the coordinate system to be as the one shown in Fig. 5, we have

$$\lim_{\alpha\to 0}\phi = \pi - (\frac{\pi}{2} - \frac{\theta}{2}) = \frac{\pi}{2} + \frac{\theta}{2}.$$

The j component of the Coulomb force is

$$F_j = k_e\frac{Ze^2\cos\phi}{r^2} = \frac{dp}{dt}, \tag{A2}$$

where ϕ and r are functions of time, also notice that p does not change along i, $k_e = 1/(4\pi\varepsilon_0)$ is the Coulomb constant. Thus, we can find again the momentum change,

$$\Delta p = \int_{-\infty}^{\infty} k_e\frac{Ze^2\cos\phi}{r^2}dt. \tag{A3}$$

From the conservation of angular momentum, we have

$$|\boldsymbol{L}| = |\boldsymbol{r}\times\boldsymbol{p}| = pb = r\gamma m r\dot{\phi} = r^2\gamma m\frac{d\phi}{dt}$$

i.e.,

$$\frac{dt}{r^2} = \frac{m\gamma}{pb}d\phi. \tag{A4}$$

Substituting Eq.(A4) into Eq.(A3), we can obtain

$$\Delta p = k_e\frac{Ze^2m\gamma}{pb}\int_{-\frac{\pi+\theta}{2}}^{\frac{\pi+\theta}{2}}\cos\phi d\phi = k_e\frac{Ze^2m\gamma}{pb}(2\cos\frac{\theta}{2}), \tag{A5}$$

where ϕ is negative when the electron is on the left and positive when it is on the right in Fig. 5, and we may approximate γ as a constant because the particle kinetic energy is much greater than the potential energy during the collision, $\gamma \gg r_e/b_{min}$.

Assuming θ is small, such that $\cos(\theta/2)\approx 1$, $\sin(\theta/2)\approx\theta/2$, and also the velocity of electron is close to the speed of light, $p = m\gamma v \approx m\gamma c$, Eq. (A1) and Eq. (A5) yield

$$\theta = \frac{2Zr_e}{\gamma b}. \tag{A6}$$

From $\theta_x = \theta\cos\varphi$, where φ is the angle between x-axis and the transverse momentum $\boldsymbol{p}_\perp$,

$$\langle\theta_x^2\rangle = \langle\theta^2\rangle\langle\cos^2\varphi\rangle = \frac{1}{2}\langle\theta^2\rangle. \tag{A7}$$

Then, we integrate over a cylindrical volume of ions with density n_i, to obtain

$$\langle\theta_x^2\rangle = \int\int\theta_x^2 n_i(2\pi b)dbdz. \tag{A8}$$

And with Eq.(A7) and Eq.(A6)

$$\begin{aligned}\frac{d\langle\theta_x^2\rangle}{dz} &= \int\theta_x^2 n_i(2\pi b)db = \frac{1}{2}\int\theta^2 n_i(2\pi b)db\\ &= \frac{4\pi n_i Z^2 r_e^2}{\gamma^2}\int\frac{db}{b} = \frac{4\pi n_i Z^2 r_e^2}{\gamma^2}\ln\Lambda,\end{aligned} \tag{A9}$$

where $\ln\Lambda = \int db/b$ is the Coulomb logarithm.

Appendix B: Derivation of the emittance growth from Coulomb scattering

Let us consider a relativistic electron beam propagating along the z direction and undergoing transverse x-y focusing in a plasma bubble. The equations of motion for individual electrons, e.g. in the x direction, can be written as:

$$\frac{dx}{dz} = \frac{u_x}{\gamma}, \tag{B1}$$

$$\frac{du_x}{dz} = -\frac{k_p^2}{2}x + \sqrt{k_p^2 r_e Z\ln\Lambda}\,\eta(z), \tag{B2}$$

where $u_x = p_x/(m_e c)$ is the dimensionless momentum, and where derivatives with respect to t were replaced by derivatives with respect to z since the beam is propagating relativisticly along z ($z\approx ct$). Note that we added a stochastic term in the second equation, so as to capture the effect of Coulomb collisions. More specifically, in the second equation $\eta(z)$ is a Gaussian white noise term, so that $\langle\eta(z)\rangle = 0$, $\langle\eta(z)\eta(z')\rangle = \delta(z-z')$, where δ is the Dirac delta function. The amplitude of this second term was chosen so that it reproduces $d\langle\theta_x^2\rangle/dt = (1/\gamma^2)d\langle u_x^2\rangle/dt$ from Eq. (1), in the absence of the focusing force.

Let us now derive the envelope equations of the beam, by combining the equations of motion and averaging them over all particles.

Multiplying Eq. (B1) by $2x$ and averaging, we obtain

$$\frac{d\langle x^2\rangle}{dz} = 2\left\langle \frac{xu_x}{\gamma}\right\rangle. \tag{B3}$$

where $\langle\rangle$ denotes an ensemble average over all particles. Multiplying Eq. (B1) by u_x and multiplying Eq. (B2) by x, then adding them together and averaging, we obtain

$$\frac{d\langle xu_x\rangle}{dz} = \left\langle \frac{u_x^2}{\gamma}\right\rangle - \frac{k_p^2}{2}\langle x^2\rangle. \tag{B4}$$

To obtain $d\langle u_x^2\rangle/dz$, we consider the focusing force and the collisional force separately. (Note that a mathematically more rigorous derivation can also be carried out by applying Itô's lemma.) Considering the focusing force term only in Eq. (B2), multiplying both sides of the equation by $2u_x$ and averaging, we can obtain

$$\left(\frac{d\langle u_x^2\rangle}{dz}\right)_{focusing} = -k_p^2\langle xu_x\rangle.$$

Considering the collisional force term only in Eq. (B2), we can integrate between z and $z+\Delta z$,

$$u_x(z+\Delta z) = u_x(z) + \sqrt{k_p^2 r_e Z\ln\Lambda}\int_z^{z+\Delta z}\eta(z')dz',$$

yielding,

$$\begin{aligned}&\langle u_x^2(z+\Delta z)\rangle\\ &= \langle u_x^2(z)\rangle + k_p^2 r_e Z\ln\Lambda\int_z^{z+\Delta z}\int_z^{z+\Delta z}\langle\eta(z')\eta(z'')\rangle dz'dz''\\ &= \langle u_x^2(z)\rangle + k_p^2 r_e Z\ln\Lambda\Delta z.\end{aligned}$$

Therefore, we have

$$\left(\frac{d\langle u_x^2\rangle}{dz}\right)_{collisional} = k_p^2 r_e Z\ln\Lambda,$$

and

$$\begin{aligned}\frac{d\langle u_x^2\rangle}{dz} &= \left(\frac{d\langle u_x^2\rangle}{dz}\right)_{focusing} + \left(\frac{d\langle u_x^2\rangle}{dz}\right)_{collisional}\\ &= -k_p^2\langle xu_x\rangle + k_p^2 r_e Z\ln\Lambda.\end{aligned} \tag{B5}$$

Now, we can combine Eq. (B3), Eq. (B4), and Eq. (B5) into

$$\frac{d\varepsilon_x^2}{dz} = 2\varepsilon_x\frac{d\varepsilon_x}{dz} = \langle x^2\rangle\frac{d\langle u_x^2\rangle}{dz} + \langle u_x^2\rangle\frac{d\langle x^2\rangle}{dz} - 2\langle xu_x\rangle\frac{d\langle xu_x\rangle}{dz} \tag{B6}$$

to obtain the analytical solution of the emittance growth rate along z due to Coulomb collisions, including the effect of decoherence via energy spread,

$$\frac{d\varepsilon_x^2}{dz} = 2\varepsilon_x\frac{d\varepsilon_x}{dz} = k_p^2 r_e Z\ln\Lambda\langle x^2\rangle + 2\left(\langle u_x^2\rangle\langle\frac{xu_x}{\gamma}\rangle - \langle xu_x\rangle\langle\frac{u_x^2}{\gamma}\rangle\right). \tag{B7}$$

The term $\langle x^2\rangle$ can be evaluated analytically. Denote $\langle x^2\rangle$ by σ_x^2. From the envelope equation under a linear focusing force,

$$\frac{d^2\sigma_x}{dz^2} = \frac{\varepsilon_x^2}{\gamma^2\sigma_x^3} - k_\beta^2\sigma_x, \tag{B8}$$

we can obtain its first integral,

$$\left(\frac{d\sigma_x}{dk_\beta z}\right)^2 + \left(\frac{\varepsilon_x}{\gamma k_\beta}\right)^2\sigma_x^{-2} + \sigma_x^2 = \text{const.} \tag{B9}$$

With initial conditions $x_0 = \sigma_x(0)$ and $x_0' = d\sigma_x(0)/dz$, the general solution can be obtained as

$$\sigma_x^2 = x_m^2\left\{\frac{1+M^2}{2} + \frac{1-M^2}{2}\cos[2(k_\beta z+\phi)]\right\}, \tag{B10}$$

where

$$M = \frac{\varepsilon_x}{\gamma k_\beta x_m^2}, \tag{B11}$$

$$\phi = \tan^{-1}\left[\frac{(x_0^2-x_m^2)^{1/2}}{(x_m^2M^2-x_0)^{1/2}}\right], \tag{B12}$$

and x_m is the peak RMS beam size (such that $\sigma_x = x_m$ when $d\sigma_x/dz = 0$).

This solution indicates that the beam size oscillates between x_m and x_mM at half the betatron period. Note that for a matched beam, $M = 1$, and $\sigma_x = x_m = $ constant.

Typically, the propagation distance z will span many betatron periods such that $k_\beta z \gg 1$. Thus, one may average over the betatron oscillations, yielding

$$\langle x^2\rangle = x_m^2\frac{1+M^2}{2}. \tag{B13}$$

[1] C. B. Schroeder, E. Esarey, C. G. R. Geddes, C. Benedetti, and W. P. Leemans, "Physics considerations for laser-plasma linear colliders," Phys. Rev. ST Accel. Beams **13**, 101301 (2010).
[2] Z. Huang, Y. Ding, and C. B. Schroeder, "Compact x-ray free-electron laser from a laser-plasma accelerator using a transverse-gradient undulator," Phys. Rev. Lett. **109**, 204801 (2012).
[3] A. R. Maier, A. Meseck, S. Reiche, C. B. Schroeder, T. Seggebrock, and F. Grüner, "Demonstration scheme for a laser-plasma-driven free-electron laser," Phys. Rev. X **2**, 031019 (2012).
[4] K. Nakajima, "Towards a table-top free-electron laser." Nature Phys **4**, 92–93 (2008).
[5] P. Michel, C. B. Schroeder, B. A. Shadwick, E. Esarey, and W. P. Leemans, "Radiative damping and electron beam dynamics in plasma-based accelerators," Phys. Rev. E **74**, 026501 (2006).
[6] T. Mehrling, J. Grebenyuk, F. S. Tsung, K. Floettmann, and J. Osterhoff, "Transverse emittance growth in staged laser-wakefield acceleration," Phys. Rev. ST Accel. Beams **15**, 111303 (2012).
[7] M. Thévenet, R. Lehe, C. B. Schroeder, C. Benedetti, J.-L. Vay, E. Esarey, and W. P. Leemans, "Emittance growth due to misalignment in multistage laser-plasma accelerators," Phys. Rev. Accel. Beams **22**, 051302 (2019).
[8] J. B. Rosenzweig, A. M. Cook, A. Scott, M. C. Thompson, and R. B. Yoder, "Effects of ion motion in intense beam-driven plasma wakefield accelerators," Phys. Rev. Lett. **95**, 195002 (2005).
[9] W. An, W. Lu, C. Huang, X. Xu, M. J. Hogan, C. Joshi, and W. B. Mori, "Ion motion induced emittance growth of matched electron beams in plasma wakefields," Phys. Rev. Lett. **118**, 244801 (2017).
[10] C. Benedetti, C. B. Schroeder, E. Esarey, and W. P. Leemans, "Emittance preservation in plasma-based accelerators with ion motion," Phys. Rev. Accel. Beams **20**, 111301 (2017).
[11] Y. Y. Lau, "Classification of beam breakup instabilities in linear accelerators," Phys. Rev. Lett. **63**, 1141–1144 (1989).
[12] A. W. Chao, B. Richter, and C.-Y. Yao, "Beam emittance growth caused by transverse deflecting fields in a linear accelerator," Nuclear Instruments and Methods **178**, 1 – 8 (1980).

[13]A. A. Geraci and D. H. Whittum, "Transverse dynamics of a relativistic electron beam in an underdense plasma channel," Physics of Plasmas **7**, 3431–3440 (2000).
[14]E. S. Dodd, R. G. Hemker, C.-K. Huang, S. Wang, C. Ren, W. B. Mori, S. Lee, and T. Katsouleas, "Hosing and sloshing of short-pulse gev-class wakefield drivers," Phys. Rev. Lett. **88**, 125001 (2002).
[15]C. B. Schroeder, D. H. Whittum, and J. S. Wurtele, "Multimode Analysis of the Hollow Plasma Channel Wakefield Accelerator," Physical Review Letters **82**, 1177–1180 (1999).
[16]C. Huang, W. Lu, M. Zhou, C. E. Clayton, C. Joshi, W. B. Mori, P. Muggli, S. Deng, E. Oz, T. Katsouleas, M. J. Hogan, I. Blumenfeld, F. J. Decker, R. Ischebeck, R. H. Iverson, N. A. Kirby, and D. Walz, "Hosing Instability in the Blow-Out Regime for Plasma-Wakefield Acceleration," Physical Review Letters **99**, 255001 (2007).
[17]B. W. Montague and W. Schnell, "Multiple scattering and synchrotron radiation in the plasma beat-wave accelerator," AIP Conference Proceedings **130**, 146–155 (1985).
[18]N. Kirby, M. Berry, I. Blumenfeld, M. J. Hogan, R. Ischebeck, and R. Siemann, "Emittance growth from multiple Coulomb scattering in a plasma wakefield accelerator," in *2007 IEEE Particle Accelerator Conference (PAC)* (2007) pp. 3097–3099.
[19]C. B. Schroeder, E. Esarey, C. Benedetti, and W. P. Leemans, "Control of focusing forces and emittances in plasma-based accelerators using near-hollow plasma channels," Physics of Plasmas **20**, 080701 (2013), https://doi.org/10.1063/1.4817799.
[20]F. Pérez, L. Gremillet, A. Decoster, M. Drouin, and E. Lefebvre, "Improved modeling of relativistic collisions and collisional ionization in particle-in-cell codes," Physics of Plasmas **19**, 083104 (2012).
[21]D. Nicholson, *Introduction to Plasma Theory* (Krieger, 1992).
[22]K. Nanbu, "Theory of cumulative small-angle collisions in plasmas," Phys. Rev. E **55**, 4642–4652 (1997).
[23]K. Nanbu and S. Yonemura, "Weighted particles in Coulomb collision simulations based on the theory of a cumulative scattering angle," Journal of Computational Physics **145**, 639 – 654 (1998).
[24]N. E. Frankel, K. C. Hines, and R. L. Dewar, "Energy loss due to binary collisions in a relativistic plasma," Phys. Rev. A **20**, 2120–2129 (1979).
[25]J.-L. Vay, "Noninvariance of space- and time-scale ranges under a Lorentz transformation and the implications for the study of relativistic interactions," Phys. Rev. Lett. **98**, 130405 (2007).
[26]J.-L. Vay, A. Almgren, J. Bell, L. Ge, D. P. Grote, M. Hogan, O. Kononenko, R. Lehe, A. Myers, C. Ng, J. Park, R. Ryne, O. Shapoval, M. Thévenet, and W. Zhang, "Warp-x: a new exascale computing platform for beam-plasma simulations," (2018), 10.1016/j.nima.2018.01.035, arXiv:1801.02568.
[27]B. M. Cowan, D. L. Bruhwiler, J. R. Cary, E. Cormier-Michel, and C. G. R. Geddes, "Generalized algorithm for control of numerical dispersion in explicit time-domain electromagnetic simulations," Phys. Rev. ST Accel. Beams **16**, 041303 (2013).
[28]C.K. Birdsall and A.B. Langdon, *Plasma Physics via Computer Simulation* (IOP, 1991).
[29]J.-P. Berenger, "A perfectly matched layer for the absorption of electromagnetic waves," Journal of Computational Physics **114**, 185 – 200 (1994).
[30]J.-L. Vay, "Noninvariance of space- and time-scale ranges under a Lorentz transformation and the implications for the study of relativistic interactions," Phys. Rev. Lett. **98**, 130405 (2007).
[31]J. P. Boris, "Relativistic plasma simulation-optimization of a hybrid code," Proceeding of Fourth Conference on Numerical Simulations of Plasmas (1970).
[32]B. M. Cowan, D. L. Bruhwiler, J. R. Cary, E. Cormier-Michel, and C. G. R. Geddes, "Generalized algorithm for control of numerical dispersion in explicit time-domain electromagnetic simulations," Phys. Rev. ST Accel. Beams **16**, 041303 (2013).
[33]Y. Zhao, R. Lehe, A. Myers, M. Thévenet, A. Huebl, C. B. Schroeder, and J.-L. Vay, "Modeling of emittance growth due to coulomb collisions in plasma-based accelerators," Zenodo (2020), 10.5281/zenodo.4097055.
[34]D. H. Whittum, W. M. Sharp, S. S. Yu, M. Lampe, and G. Joyce, "Electron-hose instability in the ion-focused regime," Phys. Rev. Lett. **67**, 991–994 (1991).
[35]J.-L. Vay, J.-C. Adam, and A. Héron, "Asymmetric pml for the absorption of waves. application to mesh refinement in electromagnetic particle-in-cell plasma simulations," Computer Physics Communications **164**, 171 – 177 (2004).